

## THREE-DIMENSIONAL NUMERICAL SIMULATIONS OF THE ACOUSTIC WAVE FIELD IN THE UPPER CONVECTION ZONE OF THE SUN

K. V. PARCHEVSKY AND A. G. KOSOVICHEV

W. W. Hansen Experimental Physics Laboratory, Stanford University, 455 Via Palou, Stanford, CA 94305; kparchevsky@solar.stanford.edu

Received 2006 December 28; accepted 2007 May 24

### ABSTRACT

Results of numerical three-dimensional (3D) simulations of propagation of acoustic waves inside the Sun are presented. A linear 3D code which utilizes the realistic OPAL equation of state was developed. A modified convectively stable standard solar model with a smoothly joined chromosphere was used as a background model. A high-order dispersion relation—preserving numerical scheme was used. The top nonreflecting boundary condition established in the chromosphere absorbs waves with frequencies greater than the acoustic cutoff frequency which pass through the chromosphere, simulating a realistic situation. We simulate acousto-gravity wave fields on the Sun, generated by localized randomly distributed sources in a subphotospheric layer. Three applications for solar wave physics are presented: changes in oscillation properties due to the mechanism of wave damping, effects of nonuniform distribution of sources, and effects of nonuniform localized perturbations on wave properties. In particular, we studied two models of wave damping with leakage and with an explicit friction-type damping term in the photospheric layers and chromosphere. In both cases we were able to reproduce observed characteristics of the acoustic spectrum (line widths and amplitude distribution). We found that the suppression of acoustic sources, e.g., in sunspots, may significantly contribute to the observed power deficit. The lower sound speed in sunspot areas may cause an increase of the wave amplitude, but this effect is less important for the acoustic power distribution than the suppression of the acoustic sources.

*Subject headings:* Sun: oscillations — sunspots

### 1. INTRODUCTION

Solar 5 minute oscillations are excited by turbulent convection (mostly by downdrafts) in subsurface layers of the Sun. These oscillations consist of acoustic and surface gravity waves which have the power spectrum with a maximum around 3 mHz and a wide range of wavenumbers. The observed oscillations can be used for reconstruction of the internal structure of the Sun by methods of helioseismology. There are several methods of investigation of interaction of acoustic waves with small inhomogeneities of the background state. One of them is the time-distance approach (Duvall et al. 1993; Kosovichev 1996). The key concept of this method is measuring and inverting wave travel times. Propagation of the acoustic waves in this approach is calculated using the ray theory or the first Born approximation (Kosovichev & Duvall 1997; Kosovichev et al. 2000; Jensen et al. 2001; Couvidat et al. 2004, 2006). These approximations have been tested using simple models for point sources (e.g., Birch et al. 2001; Birch & Felder 2004), but not for realistic solar conditions, e.g., realistic stratification and random excitation sources. Such tests, which require direct numerical simulations, are important for validating inferences from time-distance helioseismology and other local helioseismology methods.

There are two main approaches to numerical simulation of solar oscillations and waves. The first one is to use realistic nonlinear simulations of solar convection. In such simulations, waves are naturally excited by convective motions. These simulations reproduce quite well the solar oscillation spectrum (Stein et al. 2004) and have been used for testing time-distance helioseismology (Georgobiani et al. 2007). This modeling is self-consistent. However, a shortcoming of this approach is that there is no freedom in choosing the type and depth of the acoustic sources and model perturbations. The second approach, which is based on the linearized Euler or magnetohydrodynamic equations describing wave propagation for a given background state (Mansour et al. 2004;

Hartlep & Mansour 2006; Khomenko & Collados 2006; Hanasoge et al. 2006; Shelyag et al. 2006), is being actively developed now. The depth and type of the acoustic sources can be specified by the researcher. The background state can be taken from nonlinear numerical simulations or by perturbing the standard solar model. In our simulations we use this second approach. We describe the numerical method and present initial simulation results.

We developed a three-dimensional (3D) code which accurately simulates propagation of the acoustic waves in the interior of the Sun and their reflection from the photosphere and chromosphere. The method uses a high-order numerical scheme which preserves the dispersion relation for short waves better than standard classical schemes. A realistic equation of state calculated by interpolation of the OPAL tables (Rogers et al. 1996) was used. In § 2.1 we give a detailed description of the underlying physics. Most of our attention is paid to developing a consistent procedure for obtaining a convectively stable background model close to the standard solar model and establishing a realistic top boundary condition based on the perfectly matched layer (PML) method. In § 2.2 we describe a semidiscrete high-order finite-difference (FD) scheme which preserves the dispersion relation of the continuous problem. We developed stable high-order numerical boundary conditions consistent with the FD scheme. In § 3 we compare numerical and analytical solutions of various one-dimensional (1D) test problems with an isothermal background model to validate the code, investigate the accuracy of the numerical scheme, and test the nonreflecting boundary conditions in a gravitationally stratified medium. In § 4 we present results of numerical three-dimensional simulations of the acoustic wave field generated by various configurations of acoustic sources. The main goals of developing this code are to study properties of solar waves for various models of excitation sources and background perturbations and to generate artificial wave fields for testing the accuracy of the Born and ray approximations and local helioseismic diagnostics of the solar interior, currently used for analysis of *SOHO* Michelson Doppler

Imager (MDI) and Global Oscillation Network Group (GONG) data. The results of these tests will be presented in future papers. The numerical simulations are carried out using parallel supercomputers at the NASA Ames Research Center.

## 2. CODE DESCRIPTION

### 2.1. Physical Background

Propagation of adiabatic acoustic waves below the solar photosphere is described by the following system of linearized Euler equations:

$$\begin{aligned} \frac{\partial \rho'}{\partial t} + \frac{\partial}{\partial x}(\rho_0 u') + \frac{\partial}{\partial y}(\rho_0 v') + \frac{\partial}{\partial z}(\rho_0 w') &= 0, \\ \frac{\partial}{\partial t}(\rho_0 u') + \frac{\partial p'}{\partial x} &= S_x, \\ \frac{\partial}{\partial t}(\rho_0 v') + \frac{\partial p'}{\partial y} &= S_y, \\ \frac{\partial}{\partial t}(\rho_0 w') + \frac{\partial p'}{\partial z} &= -g_0 \rho' + S_z, \end{aligned} \quad (1)$$

where  $x, y, z$ , and  $t$  are the Cartesian coordinates and time, respectively,  $u', v'$ , and  $w'$  are the perturbations of the  $x$ -,  $y$ -, and  $z$ -components of velocity,  $\rho'$  and  $p'$  are the density and pressure perturbations, respectively, and  $S(x, y, z, t)$  is the wave source function. Quantities with subscript 0, such as pressure  $p_0(x, y, z)$ , density  $\rho_0(x, y, z)$ , and gravitational acceleration  $g_0(z)$  correspond to the background reference model. To close the system we used an adiabatic relation between Eulerian variations of pressure  $p'$  and density  $\rho'$ ,

$$p' = a_0^2 \rho' - a_0^2 \frac{\mathcal{N}_0^2}{g_0} (\rho_0 \xi_z), \quad (2)$$

where  $a_0^2 = \Gamma_1 p_0 / \rho_0$  is the square of sound speed,  $\Gamma_1 = (\partial \log p / \partial \log \rho)_{\text{ad}}$  is the adiabatic exponent,  $\xi_z$  is the vertical displacement,  $\mathcal{N}_0$  is the Brunt-Väisälä frequency

$$\mathcal{N}_0^2 = g_0 \left( \frac{1}{\Gamma_1} \frac{d \log p_0}{dr} - \frac{d \log \rho_0}{dr} \right), \quad (3)$$

and  $r$  is the distance from the center of the Sun. So, from the background model we need only the parameters  $a_0(x, y, z)$  and  $\mathcal{N}_0^2(x, y, z)$ .

The standard solar model is convectively unstable, especially just below the photosphere, where the temperature gradient is superadiabatic and convective motions are very intense and turbulent. Using the original standard model as a background state leads to instability of the solution of the linear system of equations (1). The convective instability is developed on a timescale of 30–40 minutes of solar time, while simulations of solar oscillations need to be performed for time intervals of at least 5–8 hr. This instability prevents this and, thus, must be suppressed. We used the standard solar model S (Christensen-Dalsgaard et al. 1996) with a smoothly joined model of the chromosphere from Vernazza et al. (1976) as the background model. The condition for stability against convection requires that the square of the Brunt-Väisälä frequency is positive. The profile of  $\mathcal{N}_0^2$  for the standard solar model near the solar surface is shown in Figure 1e by the solid curve. We calculated a modified profile  $\mathcal{N}_{\text{mod}}^2/g_0$  by replacing negative values of  $\mathcal{N}_0^2/g_0$  by zero or small positive numbers (about  $3 \times 10^{-5} \text{ Mm}^{-1}$ ). Combining equation (3) with the condition of hydrostatic equilibrium,

we get the following boundary value problem for modified  $\rho_0$  and  $p_0$ :

$$\begin{aligned} \frac{1}{\rho_0} \frac{d\rho_0}{dz} &= -\frac{g_0}{a_0^2} - \alpha \frac{\mathcal{N}_{\text{mod}}^2}{g_0}, \\ \frac{dp_0}{dz} &= -\rho_0 g_0, \end{aligned}$$

$$0 \leq z \leq L, \quad \rho_0(0) = \rho_s(0), \quad \rho_0(L) = \rho_s(L), \quad p_0(L) = p_s(L), \quad (4)$$

where  $L$  is the depth of the computational domain and  $z$  is the vertical coordinate with the origin at the bottom of the domain. We introduced a free parameter  $\alpha$ , which is determined from the boundary conditions matching the original solar model. Parameter  $\alpha$  does not change the condition of convective stability if it remains positive. So, the procedure to calculate a convectively stable background model close to the standard one is as follows. We smoothly join the density profiles of the standard solar model and the chromosphere, obtain the pressure profile from the condition of hydrostatic equilibrium, calculate a stable profile of  $\mathcal{N}_{\text{mod}}^2$ , and substitute it into the right-hand side of equation (4). Then, parameter  $\alpha$  and profiles of density and pressure of the modified convectively stable model are obtained as a solution of the boundary value problem from equation (4). The adiabatic exponent  $\Gamma_1$  is calculated from the realistic OPAL equation of state for the hydrogen  $X$  and heavy element  $Z$  abundances of the standard model ( $X = 0.737265, Z = 0.019628$ ). The vertical profiles of  $p_0, \rho_0, a_0, \mathcal{N}_0^2, \Gamma_1$ , and acoustic cutoff frequency

$$\omega_c^2 = \frac{a_0^2}{4H^2} \left( 1 - 2 \frac{dH}{dr} \right), \quad H^{-1} = -\frac{d \log \rho_0}{dr} \quad (5)$$

for both models (the standard one with the joined chromosphere and the modified convectively stable model) are shown in Figure 1. In this case, the lower boundary was 30 Mm deep, and parameter  $\alpha$  was approximately 0.861.

### 2.2. Numerical Algorithm

The system from equation (1) is written in the conservative form

$$\frac{\partial \mathbf{q}}{\partial t} + \frac{\partial \mathbf{F}(\mathbf{q})}{\partial x} + \frac{\partial \mathbf{G}(\mathbf{q})}{\partial y} + \frac{\partial \mathbf{H}(\mathbf{q})}{\partial z} = -\mathbf{R}(\mathbf{q}) + \mathbf{S}, \quad (6)$$

where  $\mathbf{q} = (\rho', \rho_0 u', \rho_0 v', \rho_0 w')^T$ ,  $\mathbf{R} = (0, 0, 0, g_0 \rho')^T$ ,  $\mathbf{S}$  is the source term with components  $(0, 0, 0, \Phi)^T$  corresponding to the  $z$ -component of force or  $(0, \partial \Phi / \partial x, \partial \Phi / \partial y, \partial \Phi / \partial z)^T$  for the pressure source, where  $\Phi(x, y, z, t)$  is a scalar function which describes the spatial distribution of sources and their temporal dependence. Vectors  $\mathbf{F}, \mathbf{G}, \mathbf{H}$ , and  $\mathbf{R}$  are linear in  $\mathbf{q}$ , and their explicit expressions can be easily found from system (1). We use a semidiscrete numerical scheme. In the semidiscrete approach, the space and time discretization processes are separated. First, the spatial discretization using a uniform grid is performed, leaving the problem continuous in time. The spatial derivatives are approximated by the FD scheme using a symmetrical seven-point stencil

$$\left. \frac{\partial f}{\partial x} \right|_m \simeq \frac{1}{\Delta x} \sum_{j=-3}^3 b_j f_{m+j} = \frac{1}{\Delta x} \sum_{j=-3}^3 b_j f(x_m + j\Delta x), \quad (7)$$

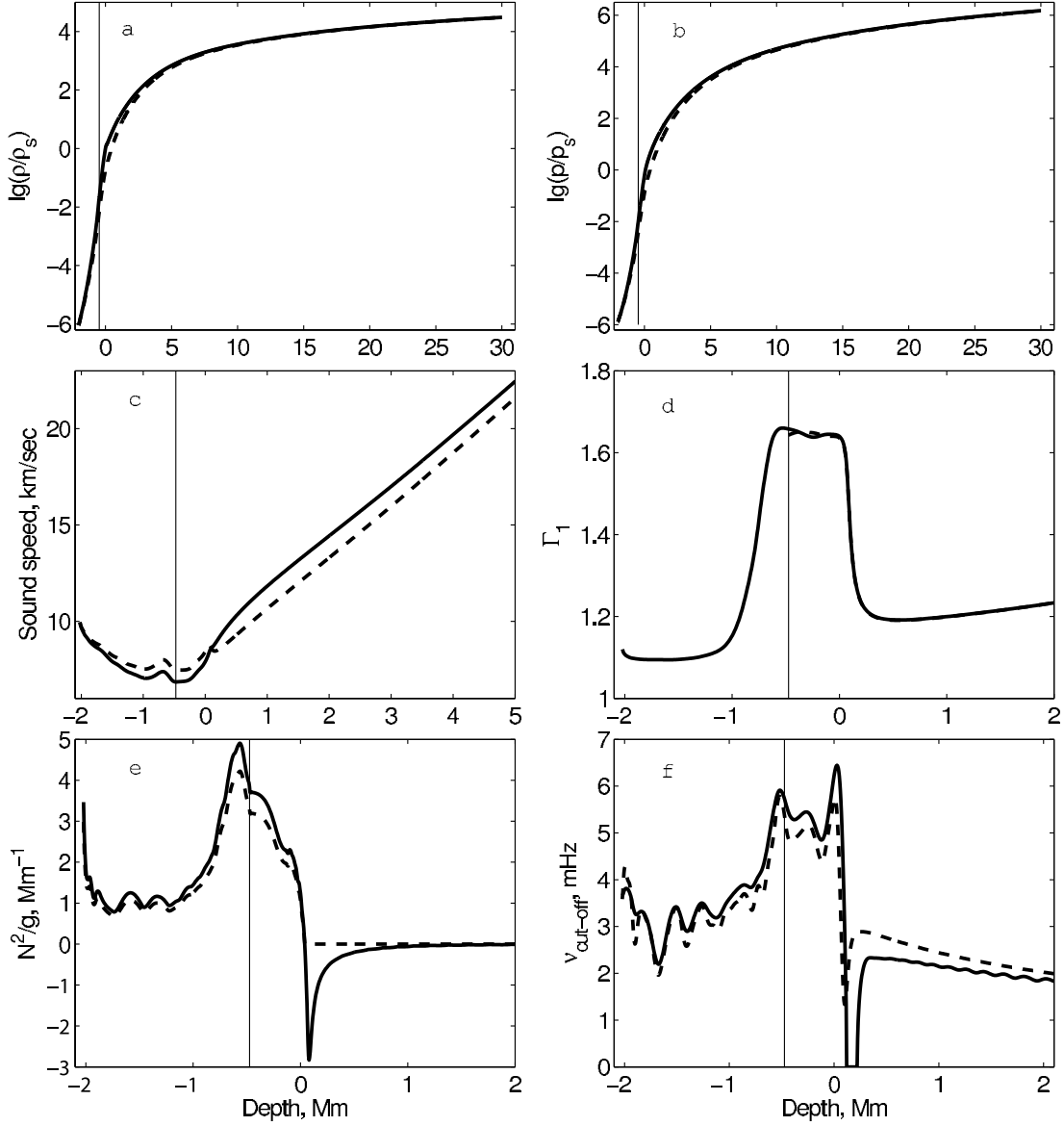


FIG. 1.—Vertical profiles of the density (a), pressure (b), sound speed (c), adiabatic exponent (d), Brunt-Väisälä frequency (e), and acoustic cutoff frequency (f). The solid curves represent profiles for the standard model, and dashed curve show the profiles of the convectively stable modified model. The thin vertical line marks the position of the fitting point between the chromosphere and the standard solar model.

where  $f$  is any component of vector  $\mathbf{q}$ . This reduces the system of partial differential equations to the system of ordinary differential equations

$$\begin{aligned} \frac{d\mathbf{q}_{ilm}}{dt} &= L_{ilm}(\mathbf{q}) + S_{ilm}(t), \\ L_{ilm}(\mathbf{q}) &= -\frac{1}{\Delta x} \sum_{j=-3}^3 b_j \mathbf{F}_{i,l,m+j} - \frac{1}{\Delta y} \sum_{j=-3}^3 b_j \mathbf{G}_{i,l+j,m} \\ &\quad - \frac{1}{\Delta z} \sum_{j=-3}^3 b_l \mathbf{H}_{i+j,l,m} + \mathbf{R}_{ilm}, \end{aligned} \quad (8)$$

where indices  $m$ ,  $l$ , and  $i$  number nodes of the spatial grid along the  $x$ -,  $y$ -, and  $z$ -axes, respectively, and  $\Delta x$ ,  $\Delta y$ , and  $\Delta z$  are the steps of the spatial grid along the corresponding axes. This system is solved by a four-stage, third-order strong stability-preserving Runge-Kutta method (Shu 2002) with the Courant number  $C = 2$ .

Time advancing from  $t^n$  to  $t^{n+1} = t^n + \Delta t$  is given by the following formulae:

$$\begin{aligned} \mathbf{q}^{(1)} &= \mathbf{q}^{(n)} + \frac{1}{2} \Delta t [L(\mathbf{q}^{(n)}) + S(t^n)], \\ \mathbf{q}^{(2)} &= \mathbf{q}^{(1)} + \frac{1}{2} \Delta t \left[ L(\mathbf{q}^{(1)}) + S\left(t^n + \frac{1}{2} \Delta t\right) \right], \\ \mathbf{q}^{(3)} &= \frac{2}{3} \mathbf{q}^{(n)} + \frac{1}{3} \mathbf{q}^{(2)} + \frac{1}{6} \Delta t [L(\mathbf{q}^{(2)}) + S(t^n + \Delta t)], \\ \mathbf{q}^{(n+1)} &= \mathbf{q}^{(3)} + \frac{1}{2} \Delta t \left[ L(\mathbf{q}^{(3)}) + S\left(t^n + \frac{1}{2} \Delta t\right) \right], \end{aligned} \quad (9)$$

where  $\Delta t$  is the time step.

The high-order dispersion relation-preserving (DRP) scheme of Tam & Webb (1993) was used for spatial discretization. Coefficients  $b_j$  in this FD scheme (eq. [7]) are chosen from the requirement that the error in the Fourier transform of the spatial

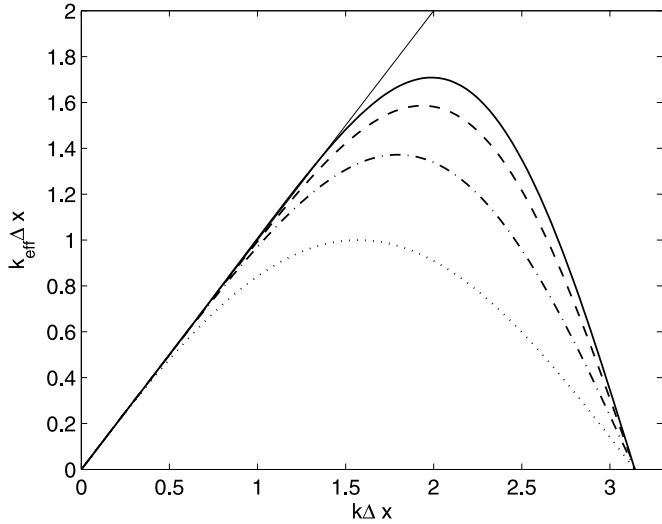


FIG. 2.— Effective wavenumber  $k_{\text{eff}} \Delta x$  vs.  $k \Delta x$  for different numerical schemes. Dotted, dash-dotted, dashed, and solid curves represent classic second-, fourth-, sixth-, and DRP fourth-order schemes, respectively.

derivative is minimal. Taking the Fourier transform from both sides of equation (7), one gets effective wavenumber  $k_{\text{eff}}$ ,

$$k_{\text{eff}} = -\frac{i}{\Delta x} \sum_{j=-3}^3 b_j e^{ijk\Delta x}. \quad (10)$$

The condition that integral error  $E = \int_{-\pi/2}^{\pi/2} |k\Delta x - k_{\text{eff}}\Delta x|^2 d(k\Delta x)$  is minimal for waves with wavelength  $\lambda \geq 4\Delta x$  can be combined with the requirement that the FD scheme from equation (7) approximates the first derivative to the fourth order. This provides a system of linear equations for  $b_j$ . The explicit expressions for this coefficients are

$$\begin{aligned} b_0 &= 0, \\ b_{\pm 1} &= \pm \frac{496 - 15\pi}{42(45\pi - 128)}, \\ b_{\pm 2} &= \mp \frac{5632 - 1725\pi}{84(45\pi - 128)}, \\ b_{\pm 3} &= \pm \frac{17(16 - 5\pi)}{14(45\pi - 128)}. \end{aligned} \quad (11)$$

The plots of numerical wavenumber  $k_{\text{eff}} \Delta x$  versus  $k \Delta x$  for different FD schemes are shown in Figure 2. Dotted, dash-dotted, dashed, and solid curves represent the classic second-, fourth-, sixth-, and DRP fourth-order FD schemes, respectively. One can see that the fourth-order DRP FD scheme describes short waves more accurately than the classic sixth-order FD scheme.

Waves with the wavelength less than  $4\Delta x$  are not resolved by the FD scheme. They lead to point-to-point oscillations of the solution that can cause a numerical instability. Such waves have to be filtered out. We used the following sixth-order digital filter to eliminate unresolved short-wave components from the solution:

$$f_i^{sm} = f_i - \beta_f \sum_{m=-3}^3 d_m f_{i+m}, \quad (12)$$

where  $f_i$  represents any component of vector  $\mathbf{q}$ ,  $f_i^{sm}$  is the corresponding filtered grid function, and  $\beta_f$  is a constant between 0 and 1 determining the filter strength. The frequency response func-

tion  $G(k)$ , which relates the Fourier images of the original  $\tilde{f}$  and filtered  $\tilde{f}^{sm}(k) = G(k)\tilde{f}(k)$  grid functions is

$$G(k\Delta x) = 1 - \beta_f \sum_{m=-3}^3 d_m e^{imk\Delta x} = 1 - \beta_f \sin^6\left(\frac{k\Delta x}{2}\right). \quad (13)$$

Then, coefficients  $d_m$  of the digital filter are symmetric and given as

$$\begin{aligned} d_0 &= 5/16, & d_1 &= d_{-1} = -15/64, \\ d_2 &= d_{-2} = 3/32, & d_3 &= d_{-3} = -1/64. \end{aligned} \quad (14)$$

The efficiency of high-order FD schemes can be reached only if they are combined with adequate numerical boundary conditions. It is easy to derive nonsymmetric boundary operators which approximate the first derivative near boundaries with high order. However, such approximations are often unstable. We follow Carpenter et al. (1993) and use an implicit Padé approximation of the spatial derivatives near the top and bottom boundaries to derive stable third-order boundary conditions (see details in the Appendix).

The spatial dependence of the acoustic source function  $S$  is given by a spherically symmetric Gaussian with a half-width of 2–3 grid nodes. The sources have a finite lifetime. We experimented with two different time dependencies of acoustic sources described by one period of the sin function,  $\sin[\omega(t - t_0)]$ ,  $t_0 \leq t \leq t_0 + 2\pi/\omega$ , and a Ricker's wavelet,  $(1 - 2\tau^2)e^{-\tau^2}$ ,  $\tau = [\omega(t - t_0)/2 - \pi]$ ,  $t_0 \leq t \leq t_0 + 4\pi/\omega$ . These time dependencies were chosen because the solar sources are not monochromatic and have spectral power localized around the central frequency  $\omega/2\pi$ , but the spectral power is not too spread out. We did simulations both with single and multiple randomly distributed sources.

Besides the numerical and convective stabilities, we have to prevent spurious reflections of acoustic waves from the boundaries. In this paper we follow Hu (1996), who proposed a perfectly matched layer (PML) procedure for Euler equations. It can be proven that for a homogeneous medium and uniform mean flow without gravity the PML absorbs waves without reflection for any angle of incidence and frequency. We set the nonreflecting boundary conditions based on the PML at the top and bottom boundaries of the domain. The lateral boundary conditions are periodic. Inside the PML, variables  $\mathbf{q}$  are split into components  $\mathbf{q}_1$ ,  $\mathbf{q}_2$ , and  $\mathbf{q}_3$  such that  $\mathbf{q} = \mathbf{q}_1 + \mathbf{q}_2 + \mathbf{q}_3$ . Thus, in the PML 3D system (1) is split into a 1D+1D+1D system of coupled, locally one-dimensional equations

$$\begin{aligned} \frac{\partial \mathbf{q}_1}{\partial t} + \frac{\partial \mathbf{F}(\mathbf{q})}{\partial x} &= 0, \\ \frac{\partial \mathbf{q}_2}{\partial t} + \frac{\partial \mathbf{G}(\mathbf{q})}{\partial y} &= 0, \\ \frac{\partial \mathbf{q}_3}{\partial t} + \frac{\partial \mathbf{H}(\mathbf{q})}{\partial z} &= -\mathbf{R}(\mathbf{q}) + \mathbf{S} - \sigma_z \mathbf{q}_3, \end{aligned} \quad (15)$$

where  $\sigma_z$  is a damping factor chosen in the form  $\Delta t \sigma_z = 0.05 + \Sigma_{\text{max}}(Z_{\text{PML}}/D)^2$ , where  $D$  is the depth of the PML and  $Z_{\text{PML}}$  is the distance from its interface with the interior domain. Values of  $\Sigma_{\text{max}}$  at the top and bottom boundaries are 0.3 and 1.0, respectively. Hu (1996) suggested to use the quadratic dependence,  $\Sigma_{\text{max}}(Z_{\text{PML}}/D)^2$ , of the damping factor on the coordinate  $Z_{\text{PML}}$ . However, in the presence of gravity the PML calculations may become unstable, and this instability develops near the interface with the interior domain, where  $\sigma_z$  is small. We found that adding a small constant term 0.05 stabilizes the PML and does

not cause noticeable reflection. It is important to note that vectors  $\mathbf{F}$ ,  $\mathbf{G}$ , and  $\mathbf{H}$  depend only on the unsplit variable  $\mathbf{q}$ . Although  $\mathbf{q}_1$ ,  $\mathbf{q}_2$ , and  $\mathbf{q}_3$  are not defined outside the PML, the variable  $\mathbf{q}$ , which is used for calculation of the spatial derivatives, is defined everywhere in the computational domain. Hence, inside the PML near the interface with the interior region we can use the same centered FD stencil as for the interior nodes. Near the top and bottom boundaries the implicit Padé approximation is used (see the Appendix), which guarantees numerical stability.

We established the top nonreflecting boundary in the chromosphere above the temperature minimum. This simulates a realistic situation when not all waves are reflected by the photosphere. Waves with frequencies higher than the acoustic cutoff frequency pass through the photosphere and are absorbed by the PML layer. Such a choice of the top boundary naturally introduces frequency dependence of its reflection properties.

### 3. NUMERICAL TESTS

For validation of the code we used a 1D initial boundary value problem (IBVP) for the linearized Euler equations with constant gravity,

$$\begin{aligned} \frac{\partial \rho'}{\partial t} + \frac{\partial}{\partial x}(\rho_0 u') &= 0, & \frac{\partial}{\partial t}(\rho_0 u') + \frac{\partial p'}{\partial x} &= g_0 \rho', \\ \frac{\partial}{\partial t}(\rho_0 \xi) &= \rho_0 u', & p' &= a_0^2 \rho' + (\Gamma_1 - 1)g_0(\rho_0 \xi), \\ 0 \leq x \leq 1, \quad t \geq 0, & \rho'(0, t) = \rho'(1, t) = 0, \\ \rho'(x, 0) &= h(x), & \rho_0(x)u'(x, 0) &= 0, \\ \rho_0(x)\xi(x, 0) &= -\int_0^x h(\eta) d\eta, \end{aligned} \quad (16)$$

where  $\xi$  is the displacement and  $x$  is the depth from the top boundary. We used nondimensional variables

$$\begin{aligned} [x, \xi] &= L, & [t] &= \frac{L}{a_0}, & [u] &= \bar{a}_0, \\ [\rho] &= \bar{\rho}_0, & [p] &= \bar{\rho}_0 \bar{a}_0^2, & [g] &= \frac{\bar{a}_0^2}{L}, \end{aligned} \quad (17)$$

where  $L$  is the depth of the computational domain and quantities with the bar represent corresponding values of the background model at the top boundary  $x = 0$ .

For test problems we chose a hydrostatic isothermal ( $p_0/\rho_0 = \text{const}$ ) background model, because it shows the characteristic behavior of a realistic solution and yet is not too complicated and can be solved analytically. The last equation of system (16) represents the adiabatic relation from equation (2) written for the isothermal background model. System (16) is written in the same conservative form as the original system (1). The analytical solution of these equations can be obtained by the method of separation of variables,

$$\begin{aligned} \rho'(x, t) &= e^{x/2H} \sum_{n=1}^{\infty} A_n \sin \pi n x \cos \lambda_n a_0 t, \\ \xi(x, t) &= e^{-x/2H} \sum_{n=1}^{\infty} B_n (\sin \pi n x - 2\pi n H \cos \pi n x) \cos \lambda_n a_0 t, \\ A_n &= 2 \int_0^1 h(\eta) e^{-\eta/2H} \sin \pi n \eta d\eta, & B_n &= -\frac{2HA_n}{1 + 4\pi^2 n^2 H^2}, \\ \lambda_n &= \sqrt{\frac{1}{4H^2} + \pi^2 n^2}, & n &= 1, 2, \dots, & H^{-1} &= \frac{\gamma g_0}{a_0^2}. \end{aligned} \quad (18)$$

The initial condition for density perturbation  $\rho'$  was chosen as

$$\rho'(x, 0) = \begin{cases} 10^4 [(x - 0.5)^2 - 0.001]^2, & 0.4 \leq x \leq 0.6, \\ 0, & x > 0.6 \text{ or } x < 0.4. \end{cases} \quad (19)$$

Solution of this problem for different moments of time for parameters  $a_0 = 1$ ,  $\Gamma_1 = 5/3$ ,  $g_0 = 10$ ,  $\Delta t = 2 \times 10^{-3}$ , and  $N = 200$  (number of grid nodes) is shown in Figure 3. The left column represents the density perturbation, and the right column shows the vertical displacement. The solid curve is the exact solution given by equation (18). The dashed curve represents the low-order solution obtained with a second-order classic central-difference approximation of spatial derivatives for the interior nodes and a first-order approximation at the boundaries (we define this scheme as CLS-2-1). The high-order numerical solution is indistinguishable from the exact one. It uses the fourth-order DRP approximation of spatial derivatives for the interior nodes with the stable third-order approximation at the boundaries (defined as DRP-4-3). The bottom panels from Figure 3 show the profiles of density and displacement after the wave reflection from the bottom boundary. This test illustrates the importance of high-order boundary conditions. No matter what the accuracy of a numerical scheme is, if boundary conditions are approximated to the first order, after reflection the accuracy of the solution switches to the first order. The high-order solution based on the DRP-4-3 scheme reproduces the exact solution quite well even after 30,000–40,000 time steps and 20–30 reflections from boundaries. This test shows that the high-order DRP numerical scheme does not introduce a noticeable damping or dispersion even for long intervals of integration. These simulations also test the accuracy and stability of the numerical boundary conditions.

To test the efficiency of the PML method for a gravitationally stratified isothermal background model, we compared the numerical solution of problem (16) for a case with the PML established at the top boundary with the exact solution of the same problem for the infinite interval  $-\infty \leq x \leq \infty$ ,

$$\begin{aligned} \rho'(x, t) &= \frac{1}{2} h(x + a_0 t) e^{-a_0 t/2H} + \frac{1}{2} h(x - a_0 t) e^{a_0 t/2H} \\ &- \frac{a_0 t}{4H} e^{x/2H} \int_{x-a_0 t}^{x+a_0 t} e^{-\eta/2H} \frac{J_1 \left[ \sqrt{a_0^2 t^2 - (x - \eta)^2} / 2H \right]}{\sqrt{a_0^2 t^2 - (x - \eta)^2}} h(\eta) d\eta. \end{aligned} \quad (20)$$

The analytical solution from equation (20) does not contain reflected waves, because all initial perturbations propagate to infinity. This solution can be used as a reference solution for determining the damping properties of the top PML. The bottom was reflecting in this test. The results for  $\rho'/(\rho_0)^{1/2}$  (scaled density perturbation to remove the exponential factor) are shown in Figure 4 for  $t = 0, 0.2, 0.4$ , and  $0.64$ . The solid curve represents the exact solution from equation (20), the dash-dotted curve represents the numerical solution with PML at the top boundary, and the dashed curve represents the exact solution from equation (18) for the reflecting top boundary. The solid vertical line marks position of the interface between the top PML and the inner region. The dashed vertical line shows the position of the initial perturbation. The top PML reduces the amplitude of the reflected wave by a factor of 20–40.

Since our original 3D system contains the acoustic source term, we have tested the code for the same problem from equation (16) with zero initial conditions  $\rho(x, 0) = 0$  and  $\rho_0(x)u'(x, 0) = 0$  and

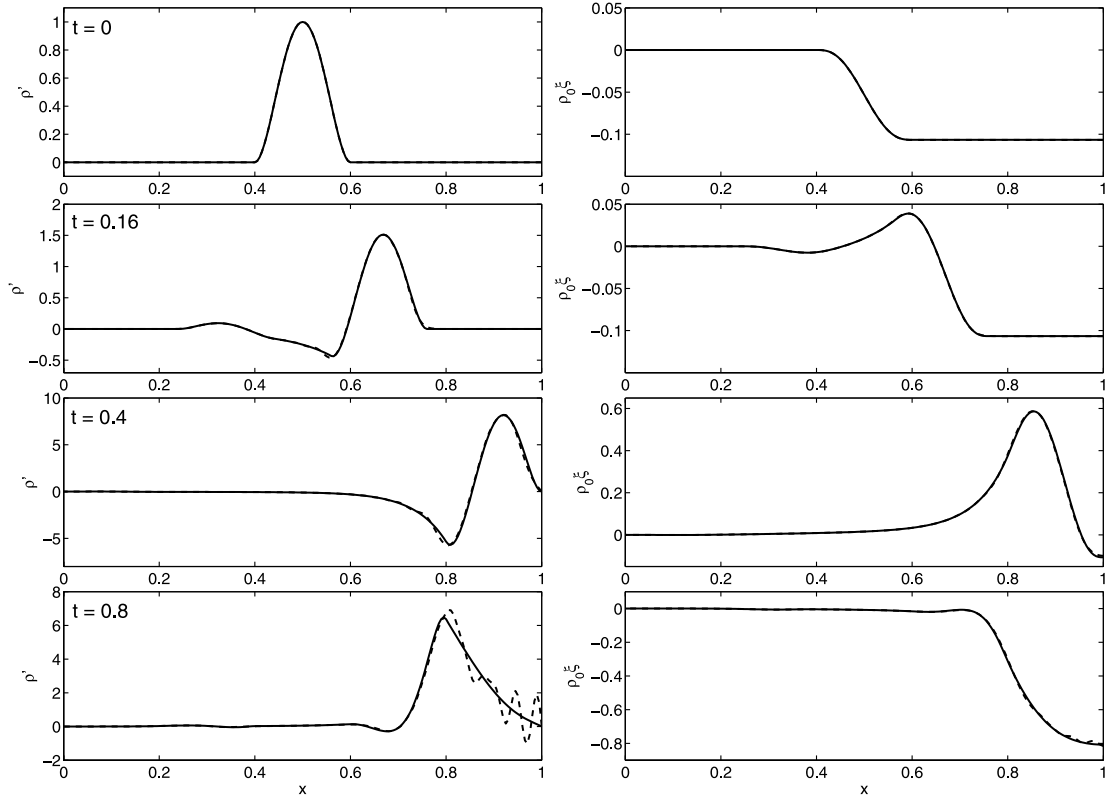


FIG. 3.— Solution of the IBVP (16) for the isothermal hydrostatic background model. Density variations and displacement are shown in the left and right panels, respectively. Solid curves represent the exact solution, and dashed curves show the CLS-2-1 numerical solution. The high-order DRP-4-3 numerical solution is indistinguishable from the exact one.

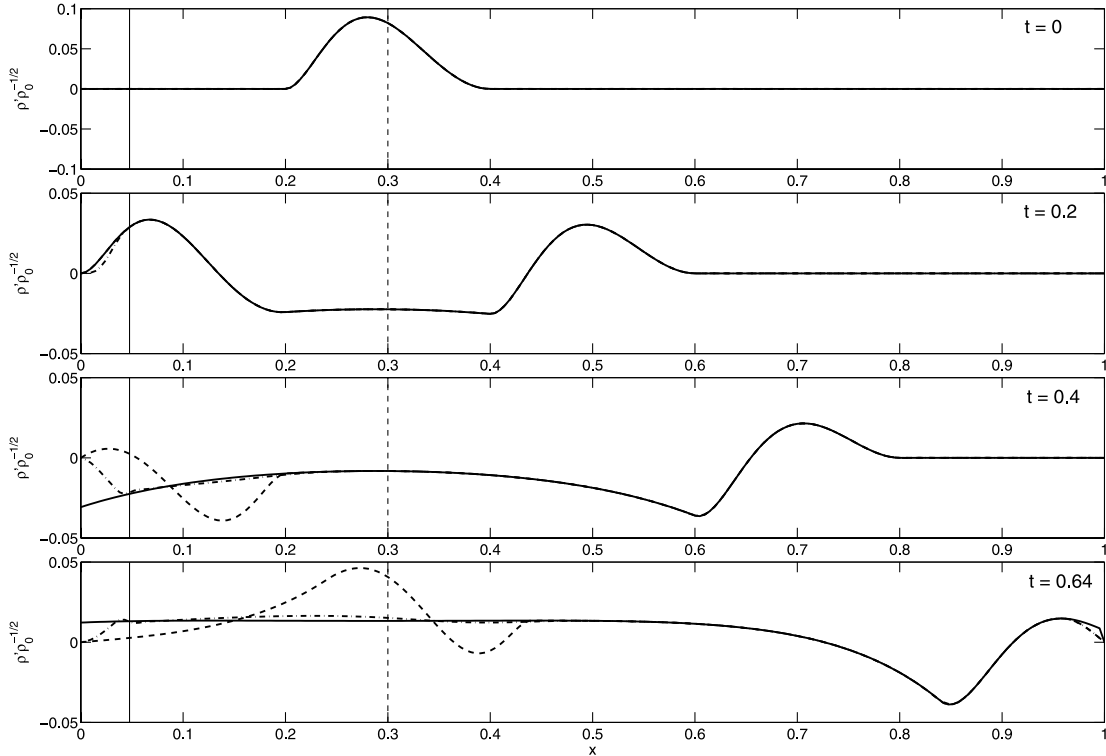


FIG. 4.— Density perturbation  $\rho'/\sqrt{\rho_0}$  for different moments of time. The solid curve represents the exact solution from eq. (20), the dash-dotted curve represents the numerical solution with the PML at the top boundary, and the dashed curve represents the exact solution from eq. (18) for the reflecting top boundary. The vertical solid and dashed lines mark positions of the PML interface and the initial perturbation, respectively.

pressure source term  $-\partial\Phi(x, t)/\partial x$  added to the right-hand side of the momentum equation, where  $\Phi(x, t)$  is a Gaussian-shaped harmonic function

$$\Phi(x, t) = \exp\left[-\left(\frac{x - h_{\text{src}}}{D_{\text{src}}}\right)^2\right] \sin(\omega_0 t), \quad (21)$$

where  $\omega_0$  is the angular frequency and  $h_{\text{src}}$  and  $D_{\text{src}}$  are the depth and spread of the source, respectively. The source amplitude is measured in units  $\bar{\rho}_0 \bar{a}_0^2$ , where the bar represents the corresponding properties of the background model at the top boundary  $x = 0$ . The analytical solution is

$$\rho'(x, t) = \int_0^t \int_0^1 \frac{\partial^2 \Phi(\eta, \tau)}{\partial \eta^2} G(x, \eta, t - \tau) d\eta d\tau, \\ G(x, \eta, \tau) = 2e^{(x-\eta)/2H} \sum_{n=1}^{\infty} \frac{\sin \lambda_n a_0 \tau}{\lambda_n a_0} \sin \pi n x \sin \pi n \eta, \quad (22) \\ \lambda_n = \sqrt{\frac{1}{4H^2} + \pi^2 n^2}, \quad n = 1, 2, \dots$$

In Figure 5 we compare this with the results of numerical simulations for parameters  $N = 120$ ,  $\Delta t = 2 \times 10^{-3}$ ,  $a_0 = 1$ ,  $\gamma = 5/3$ ,  $g_0 = 10$ ,  $h_{\text{src}} = 0.4$ ,  $\omega_0 = 10\pi$ , and  $D_{\text{src}} = 0.0178$ . The nonreflecting boundary conditions are established at the top and bottom boundaries for the numerical solution. The solid curve represents the exact solution with zero boundary conditions for  $\rho'$  at  $x = 0$  and 1. The dashed line represents the DRP-4-3 numerical solution. The vertical dashed line marks the position of the source. The vertical solid line shows the position of the interface between the interior domain and the nonreflecting PML. The numerical solution reproduces the analytical one well in the inner region and demonstrates effective damping by the absorbing layer, preventing unwanted reflection from the bottom boundary.

## 4. RESULTS AND DISCUSSION

### 4.1. Modeling of Wave Damping

In this section we present results of 3D numerical simulations of wave propagation in the solar convection zone. The convectively stabilized standard solar model (see § 2.1) with the smoothly joined chromosphere was chosen as a background model. The computational domain of  $122 \times 122 \times 32 \text{ Mm}^3$  was covered by a uniform  $816 \times 816 \times 640$  grid. The background model varies sharply in the region above the temperature minimum. Thus, to simulate propagation of acoustic waves into the chromosphere we chose the vertical spatial step  $\Delta z = 50 \text{ km}$  in order to preserve the accuracy and numerical stability. The spatial intervals in the horizontal direction are  $\Delta x = \Delta y = 3\Delta z$ . To satisfy the Courant stability condition for the explicit scheme, the time step equals 0.68 s. Spatially localized spherically symmetric sources of the  $z$ -component of force with the random amplitudes and frequencies ranging from 2 to 8 mHz were randomly distributed at the depth of 350 km below the photosphere. The sources are initiated at random moments of time (one source per time step) and depend on time as Ricker's wavelet with central frequency from range 2–8 mHz. Zero initial conditions and nonreflecting boundary conditions established at the top and bottom boundaries were used for all solar simulations. The lateral boundary conditions were periodic. The top boundary was established in the region near or above the temperature minimum. This layer absorbs all waves with frequencies higher than the acoustic cutoff frequency which pass to the chromosphere and does not affect reflection of waves with

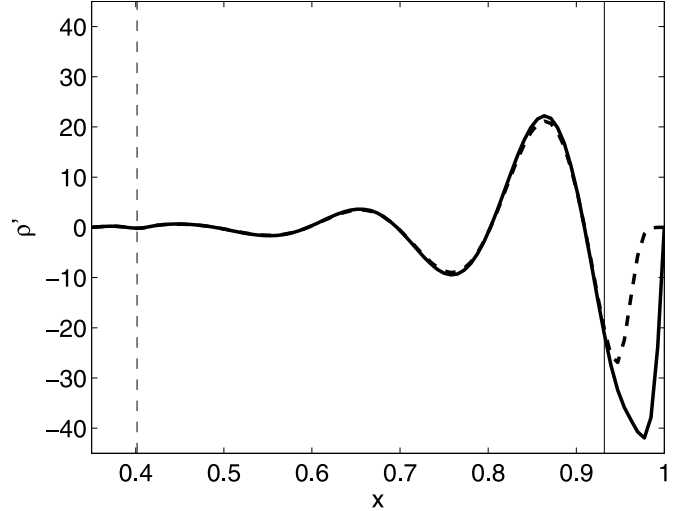


FIG. 5.—Solution of the IBVP (16) for the isothermal hydrostatic background model with the source. The solid curve represents the exact solution with zero boundary conditions for  $\rho'$ . The dashed curve represents the DRP-4-3 numerical solution with the nonreflecting top and bottom boundaries. Numerical solution is effectively damped by the absorbing layer.

lower frequencies, because these waves are reflected from lower layers below the photosphere. Such a top boundary condition naturally introduces frequency dependence of the reflection properties of the top boundary. The thickness of both the top and bottom PMLs is 250 km.

We found that the height of the PML affects the absorbing properties of the top boundary and the shape of the acoustic spectrum ( $\ell$ - $\nu$  diagram). We studied behavior of the solution for different heights of the top boundary. The region with the acoustic cutoff frequency greater than the wave frequency  $\omega_c > \omega$  acts as a potential barrier for such waves. For the low top boundary (500 km above the photosphere in our case), even if the wave frequency is less than the acoustic cutoff frequency, waves become evanescent in this region. If the thickness of the barrier is finite, then the waves can leak through it and reach the PML that causes damping. This process is similar to the tunneling effect in quantum mechanics. This happens in the real Sun as well. Balmforth & Gough (1990) found that for simulations including corona the leakage of acoustic waves into the corona has a maximum at  $\sim 8 \text{ mHz}$ . Studying the leakage of acoustic energy into the chromosphere and corona requires a separate detailed investigation and will be done in future papers. Here we are primarily focused on choosing the height of the absorbing top boundary which reproduces the properties of the solar acoustic spectrum (the line widths and the shape of the envelope).

If the height of the top boundary is sufficiently high (in our simulations it was 1750 km), the waves are reflected back from the top boundary without a noticeable damping. The modes with frequencies less than the acoustic cutoff frequency and turning points above the bottom boundary are trapped in the domain without damping. The acoustic sources continuously supply energies to the waves, and the amplitude of trapped modes is growing. The total energy increases, and the rms oscillation amplitude does not reach an equilibrium state. This distorts the acoustic power spectrum and changes the amplitude ratio of trapped modes and modes that can be absorbed at the top and/or bottom boundaries. The spectra of the vertical velocity component for observations (Fig. 6a) and the simulations with low (500 km) PML (Fig. 6b) and high (1750 km) PML (Fig. 6c) are shown in Figure 6. The left panels show the acoustic power spectra ( $\ell$ - $\nu$  diagram), and the right

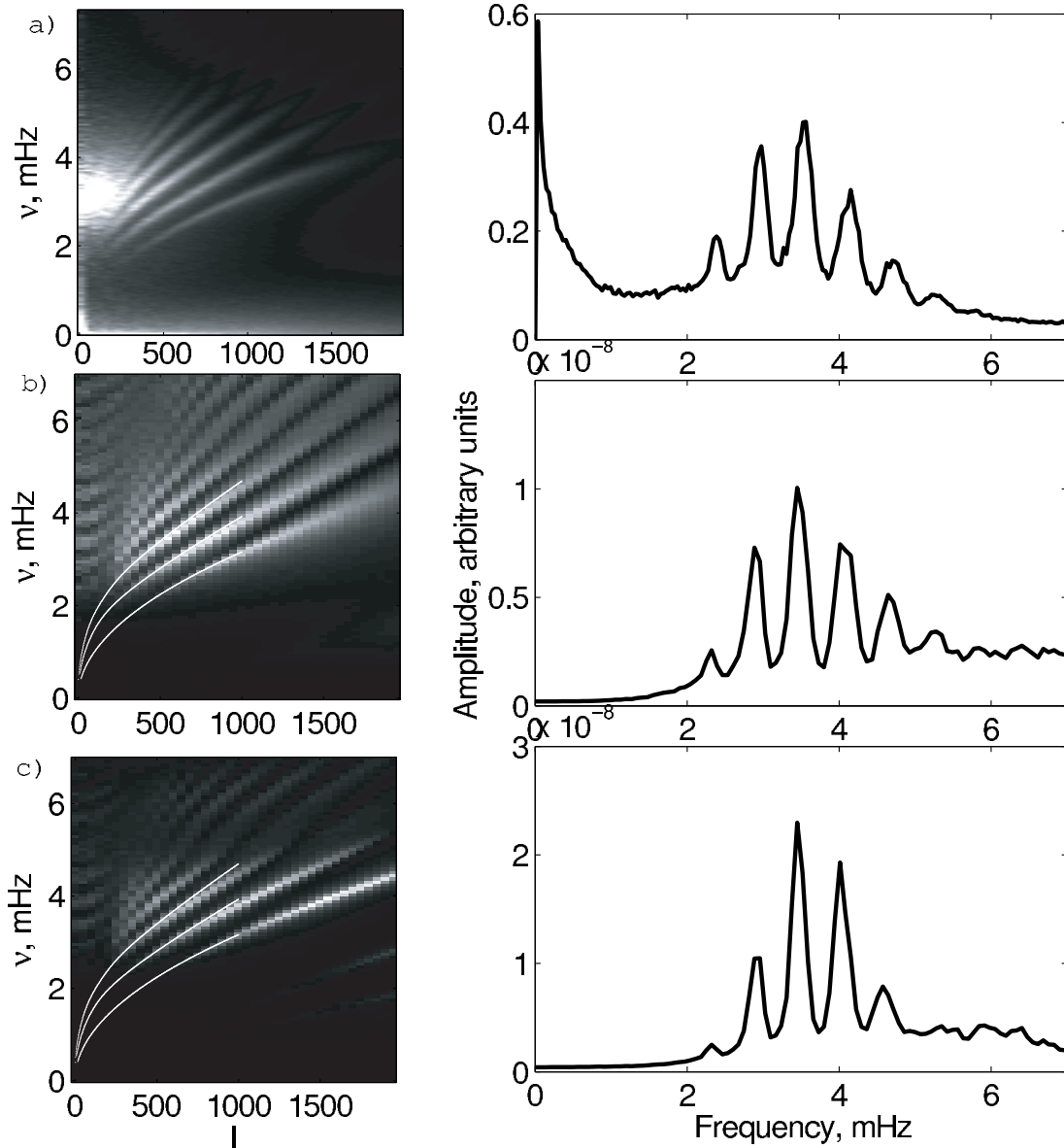


FIG. 6.—Oscillation power spectra obtained from observations (a), simulations with  $h_{\text{top}} = 500$  km (b), and simulations with  $h_{\text{top}} = 1750$  km (c). The left panels show  $\ell$ - $\nu$  diagrams, and the right panels represent cuts of corresponding diagrams at  $\ell = 584$ . The thin white curves in the left panels show the positions of the  $f$ ,  $p_1$ , and  $p_2$  ridges calculated for the modified convectively stable background model.

ones show the vertical cuts of the corresponding diagrams at  $\ell = 584$ , where  $\ell$  is the mode degree. The white curves in panels Figures 6b and 6c represent the theoretical ridges of  $f$ ,  $p_1$ , and  $p_2$  modes calculated for the modified solar model. The theoretical frequencies were calculated using the adiabatic approximation in spherically symmetric geometry by solving an eigenvalue problem for a fourth-order system of ordinary differential equations (Kosovichev 1999). Figure 6c shows the presence of weak  $g$ -modes in the simulations. They appear because our background model is made convectively stable. The acoustic spectrum obtained with the low PML (Fig. 6b) shows good agreement with observations. The envelope of the acoustic spectrum obtained with the high PML (Fig. 6c) differs from the observational one. The mode amplitudes are distorted by the trapped modes. The calculated spectral peaks are thinner than the peaks in the observed spectrum, indicating that damping in this model is weaker than on the Sun. In the case of low (500 km) PML, energy leakage through the acoustic po-

tential barrier does not change the shape (envelope) of the acoustic power spectrum. Therefore, the height of the top boundary can be used for modeling the damping rate without distortion of the envelope of the acoustic spectrum.

The damping mechanism of the solar modes below the acoustic cutoff frequency is not yet completely understood. Both interaction of acoustic waves with turbulence in subsurface layers (e.g., Gough 1980; Balmforth 1992; Murawski 2003) and non-adiabatic effects in the chromosphere (Christensen-Dalsgaard & Frandsen 1983) may play significant roles. We simulated numerically both of these mechanisms. The atmospheric damping was modeled by imposing the upper absorbing boundary at different levels. We found that the observed envelope and line widths in the power spectrum are well reproduced if we set the height of the top absorbing boundary equal to 500 km above the photosphere. Following Gizon & Birch (2002) we modeled the turbulent damping by introducing a friction-type term  $-\sigma_d(z)\rho_0 v_z$  to the vertical

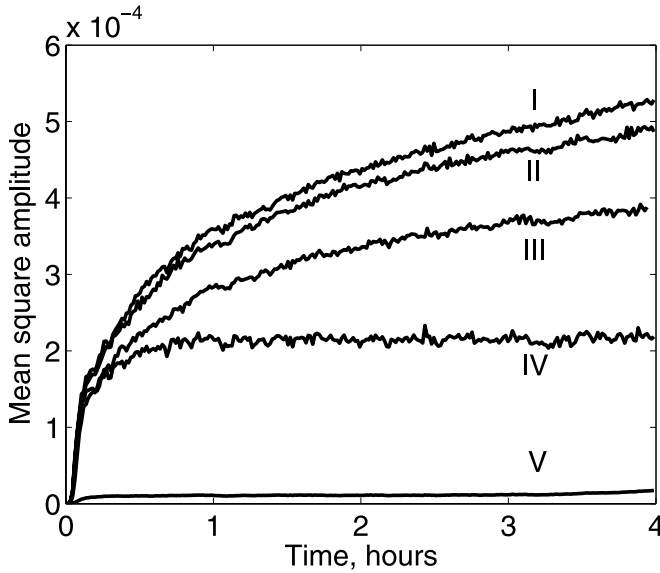


FIG. 7.—Mean square wave amplitude  $[\langle(\rho_0 w')^2\rangle_{xy}]^{1/2}/\bar{\rho}_0 \bar{a}_0$  averaged along the horizontal plane at the height of 300 km above the photosphere for different heights of the top boundary and different damping coefficients, where  $\bar{\rho}_0$  and  $\bar{a}_0$  are the density and the sound speed at the photosphere. Curve I corresponds to the high top boundary, established at 1750 km above the photosphere without any additional damping. Curves II, III, and V correspond to the same boundary conditions but different values of damping coefficient  $\sigma_d = 0.3, 0.6,$  and  $1.0$ . Curve IV corresponds to the top boundary, established at 500 km without artificial damping.

component of the momentum equation, where damping coefficient  $\sigma_d(z)$  is constant above the photosphere and smoothly decreases to zero at a depth of about 500 km. For these simulations the top absorbing boundary was established at 1750 km above the photosphere. The time dependence of the rms value of  $\rho_0 w'$  (proportional to the vertical momentum) in nondimensional units averaged over the horizontal plane at the height of 300 km above the photosphere for different heights  $h_{\text{top}}$  of the top boundary and different values of the damping coefficient  $\sigma_d$  is shown in Figure 7. Curve I represents the solution for  $h_{\text{top}} = 1750$  km and without explicit damping, and curves II, III, and V are for the same  $h_{\text{top}}$  and additional damping with  $\sigma_d = 0.3, 0.6,$  and  $1.0$ , respectively. Curve IV corresponds to the PML, established at the height of 500 km above the photosphere without additional damping in the

inner region. The rms amplitude in this case reaches an equilibrium state, because the acoustic modes leak through the acoustic potential barrier, and their evanescent parts reach the top absorbing boundary, which adds damping and stabilizes the amplitude. Numerical experiments with smaller regions of size  $200 \times 200 \times 220$  nodes and different heights of the PML show that for the PML height of 800 km the average oscillation amplitude is not stabilized. Hence, the maximum height where the PML can be established without distortion of the acoustic spectrum is the height of the temperature minimum.

From the current simulations we cannot determine the relative role of these damping mechanisms. They both can reproduce reasonably well the observed properties of the power spectrum.

#### 4.2. Nonuniform Distribution of Sources

Excitation of acoustic waves is suppressed in sunspots, because a strong magnetic field inhibits convective motions which are the source of acoustic oscillations. We randomly distributed spherically symmetric sources of the  $z$ -component of force on a horizontal plane at the depth of 350 km. For modeling the effects of suppressed excitation, we masked the wave sources (gradually reduced their strength to zero) in a circular region with the diameter of 20.4 Mm. A snapshot of the density perturbation is shown in Figures 8a and 8b. The background model has been chosen the same inside and outside the masked region. This eliminates effects of interaction of acoustic waves with perturbations of pressure and density inside the sunspot which are described in § 4.3. The acoustic waves propagate to the masked region from below by paths shown by the white dashed lines in Figure 8b. So, inside the masked region these perturbations propagate toward the photosphere and have mostly vertical velocity components. To compare oscillation amplitudes inside and outside the masked region, we calculated the oscillation power and the corresponding amplitude in these regions by doing a Fourier transform of a signal at each point of a horizontal plane at the photospheric depth and calculating an amplitude map for the chosen depth and frequency. The amplitude distribution of vertical velocity at the photospheric level for a frequency bin at  $\nu = 3.66$  mHz is plotted in Figure 8c. The thin solid curve represents a horizontal cut through the center of the masked region. The thick solid curve represents the angular-averaged amplitude. The ratio of wave amplitudes outside and inside the masked region is equal to  $2.6 \pm 0.8$ . The amplitude of oscillations drops rather sharply at the boundary of the central

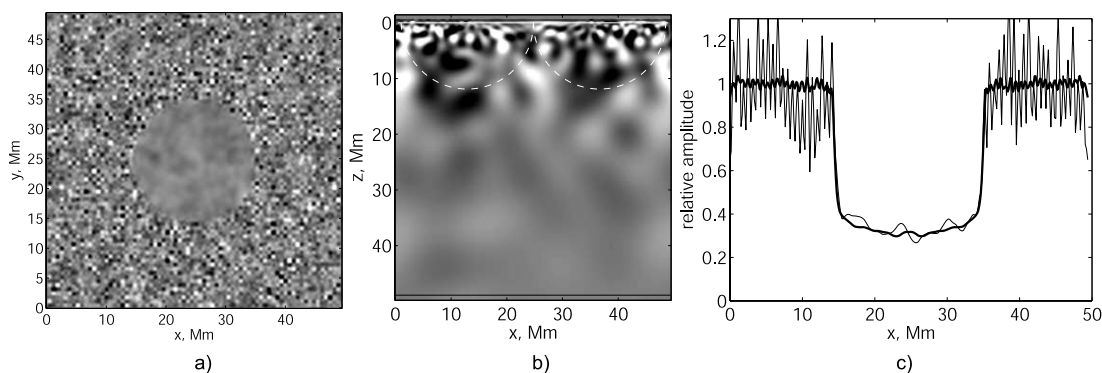


FIG. 8.—Horizontal photospheric (a) and vertical (b) slices of the density perturbation of the wave field generated by the acoustic sources masked in the central circle with the diameter of 20.4 Mm. Position of the photosphere is marked by the white horizontal line near the top boundary in (b). The thin horizontal black lines near the top and the bottom boundaries of the same panel mark the nonreflecting PMLs. Angular-averaged oscillation amplitude, calculated for the frequency  $\nu = 3.66$  mHz, is shown in (c) by the thick solid curve, and the thin solid curve represents a horizontal cut through the center of the masked region.

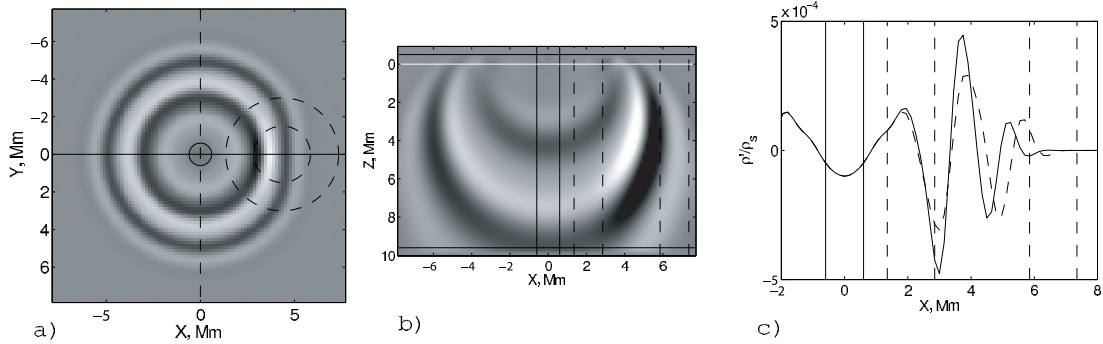


FIG. 9.—Propagation of acoustic wave generated by a single localized spherically symmetric source through an axially symmetric perturbation of the background model with reduced sound speed. Panel (a) represents a horizontal slice at the photospheric level shown by the horizontal white line in panel (b), which represents a vertical slice of the computational domain. The solid and dashed curves in panel (c) represent, respectively, horizontal and vertical cuts shown in panel (a) by the horizontal solid and vertical dashed lines. The dashed circular contour lines in panel (a) show the outer boundary of the sound speed perturbation and the level where its amplitude is half of the maximum amplitude.

region. This simulation shows that the nonuniform distribution of the acoustic sources affects the amplitude distribution of the resulting wave field and must be taken into account in sunspot seismology. Of course, additional factors such as mode conversion in magnetic field and temperature and density change may also affect the oscillation amplitude and have to be included in future simulations.

#### 4.3. Interaction with Inhomogeneities of Solar Structure

To study the effects of 3D inhomogeneous structures, we simulated propagation of waves, generated by a single spherically symmetric source of the  $z$ -component of force, through an axially symmetric region with reduced sound speed

$$a_{\text{sp}}^2(x, y, z) = a_0^2(z) \left[ 1 - \frac{\delta a^2}{\bar{a}_0^2} \Big|_{\text{ph}} Q(r_h) \cos \frac{\pi z}{2H_{\text{sp}}} \right], \quad (23)$$

where  $r_h = [(x - x_c)^2 + (y - y_c)^2]^{1/2}$  is the horizontal distance from the axis  $(x_c, y_c)$  of the sound speed perturbation,  $(\delta a^2 / \bar{a}_0^2)_{\text{ph}}$  is the relative perturbation of the square of sound speed at the photospheric level,  $H_{\text{sp}}$  is the depth of the inhomogeneity, and the horizontal profile of the sound speed perturbation  $Q(x, y)$  is given by

$$Q(x, y) = \begin{cases} \frac{1}{2} \left( 1 + \cos \frac{\pi r_h}{R_{\text{sp}}} \right), & r_h \leq R_{\text{sp}}, \\ 0, & r_h > R_{\text{sp}}, \end{cases} \quad (24)$$

where  $R_{\text{sp}}$  is the radius of the perturbation. The source function depends on time as Ricker's wavelet. The maps of density perturbation  $\rho'$  at 10.8 minutes after switching on the source are presented in Figure 9. Figures 9a and 9b show photospheric horizontal and vertical slices, respectively. The white horizontal line near the top boundary in Figure 9b marks the position of the photosphere. The position of the background sound speed perturbation is shown by the dashed circles in Figure 9a and the vertical dashed lines in Figure 9b. The outer circle corresponds to the radius  $R_{\text{sp}}$ , and the inner one shows a half-width level of the profile. The small solid circle near the center of Figure 9a shows the wave source. The solid curve in Figure 9c represents a horizontal cut through the center of the sunspot (marked by the solid horizontal line in Fig. 9a), the dashed curve shows a vertical cut marked in Figure 9a by the dashed line. The vertical solid and dashed lines in Figure 9c show the positions of the source and the sunspot, respectively. The

vertical cut is used as a reference profile because it goes through parts of the wave front not perturbed by the sunspot. This calculation shows that the sound speed perturbation results in delaying the wave front and increasing its amplitude by 20%. Thus, such an effect can be measurable by local helioseismology.

## 5. CONCLUSION

We developed a linear 3D code for modeling propagation of acoustic waves inside the Sun. The code utilizes the realistic equation of state by interpolation of the OPAL tables, the non-reflecting boundary conditions based on PML, and stable high-order numerical boundary conditions consistent with the interior FD scheme. The top nonreflective boundary above the temperature minimum naturally introduces frequency dependence of the reflecting properties of the top boundary and simulates a realistic situation when waves with frequencies less than the acoustic cut-off frequency are reflected from the photosphere and waves with higher frequencies escape into the chromosphere. The wave sources are modeled by stochastic randomly distributed perturbations of force and pressure. The accuracy of this code has been extensively tested by using analytical solutions for gravity-acoustic waves. We have presented initial results of three studies for solar acoustic waves. The first one is simulations of oscillation power spectra for two models of wave damping with leakage and damping in the lower chromosphere and with an explicit damping (friction-type) term in the subphotospheric layers and chromosphere. In both cases, we were able to reproduce the observed characteristics (line widths and amplitude distribution in the acoustic spectrum). The second study was to model nonuniform distribution of sources. In this case, we found that the suppression of acoustic sources in sunspots may significantly contribute to the observed power deficit. The third study was to investigate the effects of localized perturbations of temperature on wave properties. It showed that the temperature reduction in sunspots may lead to higher amplitude, but this effect is less significant than the effect of suppressed excitation. All these effects are important for local helioseismology and deserve future detailed investigation, using both observations and simulations.

This research is supported by the Living With the Star NASA grant NNG 05-GM85G. The calculations were performed on the Columbia supercomputer at NASA Ames Research Center.



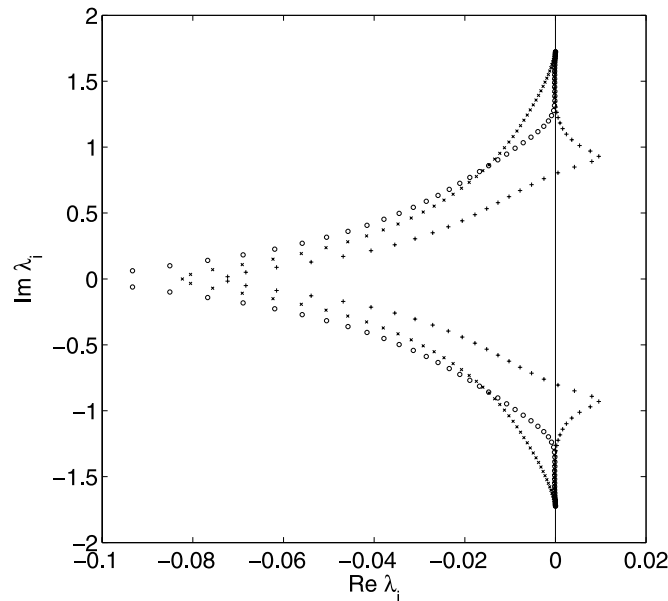


FIG. 10.—Eigenvalues of the DRP spatial discretization operator for the scalar advection equation on complex plane for different choices of the coefficient  $p_{23}$ . Plus symbols correspond to the FD scheme with  $p_{23} = 1/30$  and  $p_{33} = 31/32$ , which does not exhibit an asymptotic stability. Circles and crosses represent choices of  $p_{23} = 1/90$  and  $-1/10$  and  $p_{33} = 125/128$  and  $65/64$ , respectively. Both these FD schemes are asymptotically stable.

To satisfy the condition of positive definiteness, it is sufficient to choose matrix elements  $p_{33}$  and  $p_{23}$  in such a way that the signs of coefficients of a characteristic polynomial alternate. However, this property does not guarantee that the solution is bounded for all times. This property is known as asymptotic stability. To make a solution asymptotically stable, all eigenvalues of the spatial discretization operator  $L_{ilm}$ , represented by equation (8) with the boundary conditions, must have nonpositive real parts. Because of the complexity of the original 3D problem, we have tested the stability of the FD scheme using a 1D advection problem. The distribution of eigenvalues of the DRP spatial discretization operator in the complex plane for different choices of the pairs of coefficients  $(p_{23}, p_{33})$  is shown in Figure 10. Plus symbols correspond to the scheme  $p_{23} = 1/30$ ,  $p_{33} = 31/32$ , which does not exhibit asymptotic stability. Circles and crosses represent choices  $(1/90, 125/128)$  and  $(-1/10, 65/64)$  of coefficients  $(p_{23}, p_{33})$ , respectively. Both these FD schemes are asymptotically stable.

#### REFERENCES

- Balmforth, N. J. 1992, *MNRAS*, 255, 603  
 Balmforth, N. J., & Gough, D. O. 1990, *ApJ*, 362, 256  
 Birch, A. C., & Felder, G. 2004, *ApJ*, 616, 1261  
 Birch, A. C., Kosovichev, A. G., Price, G. H., & Schlottmann, R. B. 2001, *ApJ*, 561, L229  
 Carpenter, M. H., Gottlieb, D., & Abarbanel, S. 1993, *J. Comput. Phys.*, 108, 272  
 Christensen-Dalsgaard, J., & Frandsen, S. 1983, *Sol. Phys.*, 82, 165  
 Christensen-Dalsgaard, J., et al. 1996, *Science*, 272, 1286  
 Couvidat, S., Birch, A. C., & Kosovichev, A. G. 2006, *ApJ*, 640, 516  
 Couvidat, S., Birch, A. C., Kosovichev, A. G., & Zhao, J. 2004, *ApJ*, 607, 554  
 Duvall, T. L., Jr., Jefferies, S. M., Harvey, J. W., & Pomerantz, M. A. 1993, *Nature*, 362, 430  
 Georgobiani, D., Zhao, J., Kosovichev, A., Benson, D., Stein, R. F., & Nordlund, Å. 2007, *ApJ*, 657, 1157  
 Gizon, L., & Birch, A. C. 2002, *ApJ*, 571, 966  
 Gough, D. 1980, in *Nonradial and Nonlinear Stellar Pulsation*, ed. H. A. Hill & W. A. Dziembowski (Berlin: Springer), 273  
 Hanasoge, S. M., et al. 2006, *ApJ*, 648, 1268  
 Hartlep, T., & Mansour, N. 2006, *BAAS AAS Sol. Phys. Meet.*, 37, 5.12  
 Hu, F. Q. 1996, *J. Comput. Phys.*, 129, 201  
 Jensen, J. M., Duvall, T. L., Jr., Jacobsen, B. H., & Christensen-Dalsgaard, J. 2001, *ApJ*, 553, L193  
 Khomenko, E., & Collados, M. 2006, *ApJ*, 653, 739  
 Kosovichev, A. G. 1996, *ApJ*, 461, L55  
 ———. 1999, *J. Comput. Appl. Math.*, 109, 1  
 Kosovichev, A. G., & Duvall, T. L., Jr. 1997, in *SCORE '96: Solar Convection and Oscillations and Their Relationship*, ed. F. P. Pijpers, J. Christensen-Dalsgaard, & C. S. Rosenthal (Dordrecht: Kluwer), 241  
 Kosovichev, A. G., Duvall, T. L., Jr., & Scherrer, P. 2000, *Sol. Phys.*, 192, 159  
 Mansour, N. N., Kosovichev, A. G., Georgobiani, D., Wray, A., & Miesch, M. 2004, in *Proc. SOHO 14/GONG 2004 Workshop*, ed. D. Danesy (ESA SP-559; Noordwijk: ESA), 164  
 Murawski, K. 2003, in *Contributions to NATO Advanced Research Workshop Turbulence, Waves, and Instabilities in the Solar Plasma*, Vol. 13, ed. R. Erdélyi, E. Forgács-Dajka, & K. Petrovay (Budapest: PADEU), 61  
 Rogers, F. J., Swenson, F. J., & Iglesias, C. A. 1996, *ApJ*, 456, 902  
 Shelyag, S., Erdélyi, R., & Thompson, M. J. 2006, *ApJ*, 651, 576  
 Shu, C.-W. 2002, in *Collected Lectures on the Preservation of Stability under Discretization*, ed. D. Estep & S. Tavener (Philadelphia: SIAM), 51  
 Stein, R., Georgobiani, D., Trampedach, R., Ludwig, H.-G., & Nordlund, Å. 2004, *Sol. Phys.*, 220, 229  
 Tam, C., & Webb, J. 1993, *J. Comput. Phys.*, 107, 262  
 Vernazza, J. E., Avrett, E. H., & Loeser, R. 1976, *ApJS*, 30, 1